Loss and decoherence in superconducting circuits on silicon: Insights from electron spin resonance

Aditya Jayaraman,* Andrey V. Danilov, Jonas Bylander, and Sergey E. Kubatkin
Department of Microtechnology and Nanoscience MC2, Chalmers University of Technology, SE-41296 Goteborg, Sweden

(Received 16 February 2024; revised 13 May 2024; accepted 14 June 2024; published 12 July 2024)

Solid-state devices used for quantum computation and quantum sensing applications are adversely affected by loss and noise caused by spurious, charged two-level systems (TLS) and stray paramagnetic spins. These two sources of noise are interconnected, exacerbating the impact on circuit performance. We use an on-chip electron spin resonance (ESR) technique, with niobium nitride (NbN) superconducting resonators, to study surface spins on silicon and the effect of postfabrication surface treatments. We identify two distinct spin species that are characterized by different spin-relaxation times and respond selectively to various surface treatments (annealing and hydrofluoric acid). Only one of the two spin species has a significant impact on the TLS-limited resonator quality factor at low-power (near-single-photon) excitation. We observe a three- to fivefold reduction in the total density of spins after surface treatments and demonstrate the efficacy of ESR spectroscopy in developing strategies to mitigate loss and decoherence in quantum systems.

DOI: 10.1103/PhysRevApplied.22.014030

I. INTRODUCTION

Contemporary solid-state devices for quantum computation and quantum sensing suffer from energy loss and noise originating from materials defects [1–3]. Predominantly located in dielectrics within the devices, these fluctuators cause quantum decoherence, which prevents reaching the performance level necessary for meaningful applications [3]. For superconducting devices—a leading platform for quantum computation—it is widely accepted that all interfaces (substrate-air, substrate-metal, and metal-air) host spurious defects that manifest as two-level systems (TLSs) [1,4–9]. Despite decades of research on TLSs, their microscopic nature has remained elusive and mitigation strategies have been largely empirical: to remedy this, we seek an improved understanding of the origin of these defects and informed strategies for their removal during or after device fabrication.

TLSs can exhibit an electric dipole moment, resulting in charge noise and energy loss in superconducting resonators and qubits [2,10–14]. Noise with a $1/f$ -type spectrum is comprehensively explained by the generalized tunneling model (GTM), which considers the dipole-dipole interaction between the TLSs [15]. The GTM distinguishes between two different types of fluctuators: coherent quantum two-level systems (cTLSs) and incoherent classical two-level fluctuators (TLFs). While resonant cTLSs are responsible for energy loss in resonators, the slowly fluctuating TLFs impart an energy drift on the resonant cTLSs, resulting in charge (dielectric) noise.

Similarly, TLSs can possess spin, which is a source of magnetic flux noise [16–19]; the $1/f$ noise observed in flux qubits and superconducting quantum interference devices (SQUIDs) occurs as a result of the coupling to stray spins. Several types of spin defects, such as surface dangling bonds [20], adsorbed molecules [21–23], and intrinsic nuclear spins [24], have been proposed as potential sources of flux noise. While the standard tunneling model (STM) and GTM can also be used to effectively model environments dominated by spins, the predominant mechanisms of energy loss are attributed to charge defects, which interact more significantly with the resonator field [25]. Nonetheless, most of the surface defects possess both charge (or electric dipole) and spin, resulting in a potentially more intricate effect on quantum devices.

Silicon and sapphire are substrate materials commonly used for superconducting quantum devices. Recent studies of sapphire suggest that paramagnetic surface spins act as TLFs and their removal leads to reduced charge noise in resonators, underscoring the importance of spins in the context of quantum circuit performance [10,26].

*Contact author: adityaja@chalmers.se

In this work, we employ an on-chip electron-spin resonance (ESR) technique to identify the composition of dilute spins on intrinsic silicon (Si), the most popular substrate for high-coherence superconducting qubits. Our ESR spectra reveal two distinct spin families residing on the silicon surface. Further measurements to determine the corresponding dissipative losses allow us to associate one family with coherent (cTLS) and the other with noncoherent (TLF) fluctuators. We demonstrate that moderate annealing of the chip selectively removes TLFs, while treatment with hydrofluoric acid (HF) removes spins associated with cTLSs; these two postfabrication treatments therefore target different contributing sources to the decoherence pathway.

II. DEVICE DESCRIPTION

The resonators used in this work are descendants of a design reported by de Graaf [27], shown in Fig. 1(a), with a "quasifractal" geometry optimized for high sensitivity to surface spins in ESR measurements [21,28–30] (rather than to obtain the highest possible Q factor). The circuits have been etched out of a 120-nm-thick NbN film sputtered onto an intrinsic silicon substrate and patterned using electron-beam lithography (see Appendix A).

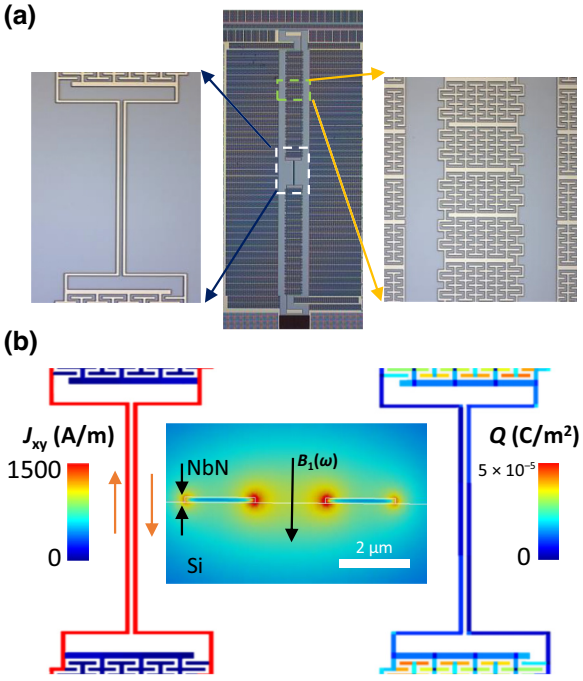

FIG. 1. (a) An optical image of an NbN resonator with narrow strip lines at its center. (b) A SONNET simulation showing the microwave current-density (J_{xy}, left) and charge-density (Q, right) distribution at the current antinode. The microwave magnetic field (B_1) is primarily confined to a small area between the strip lines (center).

The fundamental harmonic of the resonator is a half-wavelength ($\lambda/2$) mode, which has a current antinode at the center. The antinode region comprises a pair of superconducting strips measuring 2 μm in width, with a spacing of 2 μm. The magnetic fields generated by the strips interfere constructively between the strips and destructively elsewhere, so that the microwave field is effectively confined to a micrometer-scale volume, as illustrated in the inset of Fig. 1(b). Consequently, the resonator couples primarily to the surface spins in this area and its surface spin resolution is about 10^5–10^6 spins/mm^2.

III. RESULTS

A. ESR spectra

A typical ESR spectrum measured using an NbN resonator on silicon is presented in Fig. 2(a) (red). The plot represents the field-dependent part of the total energy losses in the resonator, $Q_B^{-1}(B) = Q_i^{-1}(B) - Q_i^{-1}(0)$, where the internal Q factor (Q_i) is extracted from the S_{21} resonance data as a function of the applied parallel magnetic field (B). The spectrum measured on silicon (red) is in contrast with that on sapphire [see Fig. 2(a), black]. On silicon, we observe a pronounced sharp peak

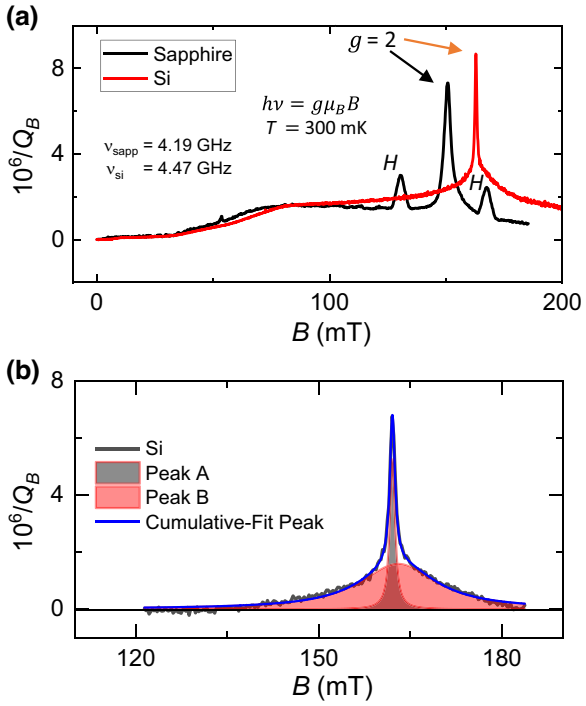

FIG. 2. (a) ESR spectra of surface spins on silicon (red) and sapphire (black) measured at $T = 300$ mK with an NbN resonator [21]. The salient features, including the hydrogen satellite peaks (in the sapphire spectrum) and the central $g = 2$ peak, are labeled. (b) The $g = 2$ region of the spectrum (linear background subtracted), showing the decomposition into two Lorentzian peaks (A and B) with different line widths.

corresponding to a spin ensemble with a g factor $g = 2$. The line width of the peak (1.2 mT), however, is less than that on sapphire (5 mT), implying the presence of more coherent $g = 2$ spins on silicon. Interestingly, both the silicon and sapphire peaks are superimposed on a broad background pedestal with an onset at approximately 50 mT. Moreover, on sapphire, the spectrum reveals the presence of atomic hydrogen on the surface, as evidenced by the presence of additional satellite peaks with a separation (ΔB) corresponding to 1.42 GHz [10,21,26]. The absence of satellite peaks on silicon suggests that atomic hydrogen is not adsorbed on its surface (and also indicates that it is not adsorbed on the surface of NbN in both devices). This could be attributed to the lower adsorption energy of hydrogen on silicon relative to sapphire, although hydrogen is known to passivate surface defects on silicon [31].

While the central $g = 2$ peak in the sapphire spectrum can be fitted with a single Lorentzian [21], the silicon spectrum cannot—instead, it requires two peaks with different line widths [see Fig. 2(b)]. This indicates the presence of two distinct spin communities, both of which possess the same g factor. The line width of the sharper peak (A) is $\gamma_2/2\pi = g\mu_B\Delta B/h = 33$ MHz, whereas that of the wider peak (B) is 670 MHz (here, μ_B is the Bohr magneton and h is Planck's constant). Assuming that the peaks are homogeneously broadened, as indicated by faithful Lorentzian fits, the spin relaxation times (T_2) can be directly estimated from the line widths and are found to be 30 ns for peak A and 1.5 ns for peak B.

We will now explore the impact of surface treatments on the two types of identified spin groups (from here on, referred to as "type-A" and "type-B" spins, corresponding to peaks A and B). Two specific surface treatments have been carried out on the silicon sample: annealing at 300 °C for 30 min in vacuum and submersion in a 5% HF solution; the latter has been done for either 1 min or 10 min, on different samples. In Fig. 3(a), we illustrate the ESR spectrum prior to treatment as well as after each treatment. We observe that annealing causes a notable decrease in the sharp $g = 2$ peak (A) and a minor decrease in the background signal [see Fig. 3(b)], whereas HF treatment causes a reduction of peak B and a significant decline in the background signal, with the step at approximately 80 mT almost entirely disappearing; however, HF does not significantly further reduce peak A. We note that the line widths of the peaks do not change, signifying a reduced density of surface spins without any effect on the relaxation time scales (Appendix B). By calculating the integrals of the areas under the ESR spectra for each case, we can directly compare these spin densities [see the inset in Fig. 3(a)]. Following both treatments, we observe a significant three- to fivefold reduction in the total spin density. Furthermore, the separate integrated inverse areas of peaks A and B are shown in Figs. 4(a) and 4(b), respectively, calculated

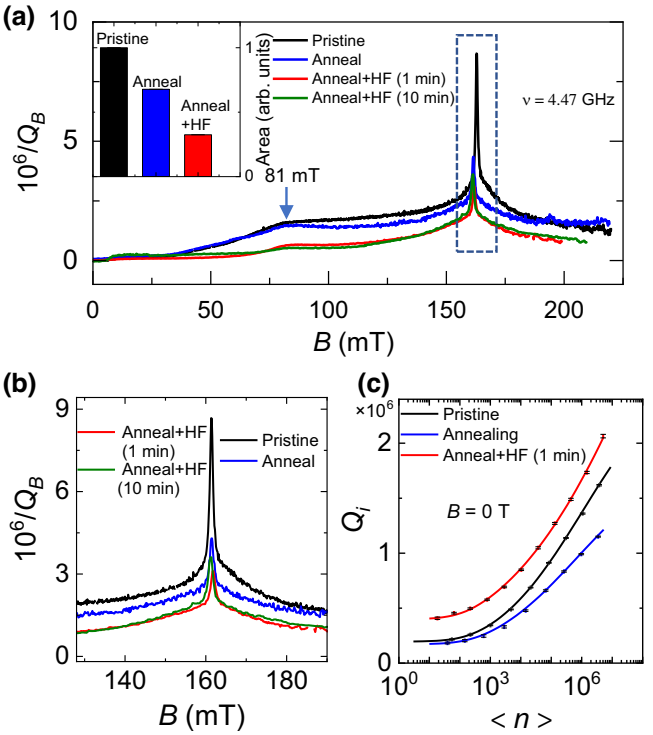

FIG. 3. (a) The ESR spectra of an NbN-on-Si resonator taken before and after surface treatments. An arrow marks the field corresponding to half of the $g = 2$ resonance. Post annealing, the $g = 2$ peak shifts slightly due to a reduction in the frequency of the resonator caused by changes in the kinetic inductance of the NbN film. The inset shows the total area of the ESR spectra before and after treatments. (b) The effect of treatments on the central $g = 2$ peak. The minor shifts in (a) are adjusted for clarity. (c) The internal Q factor (Q_i) as a function of the average photon number before and after treatments ($B = 0$). The solid lines represent fits to the TLS model in Eq. (1).

for four resonators when pristine, after annealing and HF immersion. 1/Area ($\propto 1/n$, where n is the density of each spin species) provides a direct measure of the residual spin density after each surface treatment. We observe a reduction by a factor of between 4 and 5 in the type-A spins and a factor-of-2 reduction in the type-B spins after treatments.

B. Microwave loss measurements

Although annealing and HF have different effects on the concentrations of the two types of spins, we also notice different impacts on the zero-field Q factors of the resonator, as shown in Fig. 3(c). We fit the power dependence of Q_i of the resonator according to the model for interacting TLSs [14],

$$\frac{1}{Q_i(\langle n\rangle)} = \delta_0 + \frac{1}{Q_{\mathrm{TLS}}}\left(1 + \frac{\langle n\rangle}{n_c}\right)^{-\beta}, \qquad (1)$$

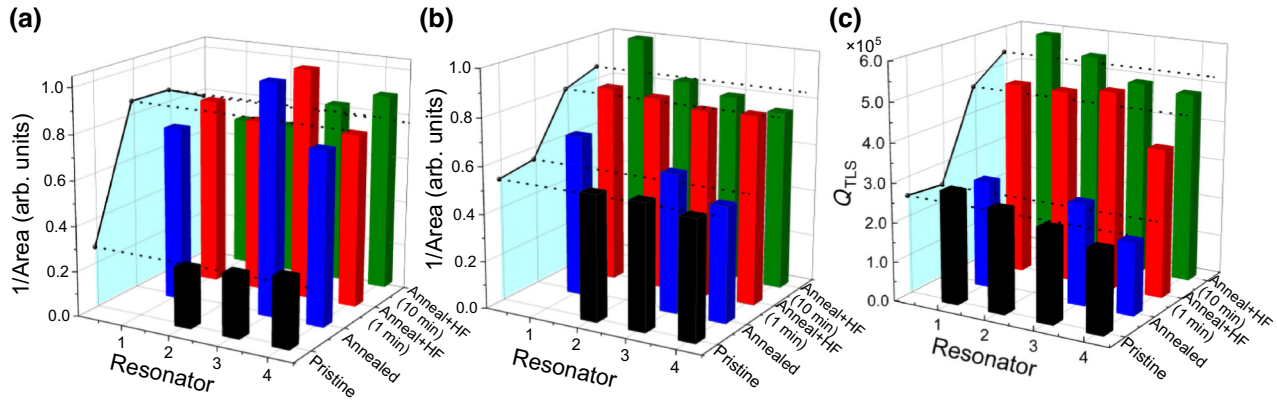

FIG. 4. The effect of annealing and HF immersion treatments on four resonators with resonant frequencies 3.88, 4.09, 4.47, and 4.90 GHz. (a),(b) The inverse area of the sharper peak A and the wider peak B, respectively. (c) The TLS-limited resonator zero-field Q factors, Q_{TLS}. The average values of Q_{TLS} and areas across all resonators are projected onto the left coordinate plane (shaded in cyan). (Some resonators have not been measurable due to interference with spurious ground-plane resonances.)

where δ_0 represents power-independent non-TLS-related dissipation, $\langle n\rangle$ is circulating power in the resonator, expressed as the mean photon population, and n_c is the average number of photons required to saturate a single TLS. The power exponent β indicates the rate at which TLSs saturate with power: it is 0.5 for noninteracting TLSs but has a smaller value in the more general case of an interacting-TLS model, and the value we extract from our data (approximately 0.2) is consistent with that reported in the literature [10,14,15].

Following annealing, we observe a minimal change in the TLS-limited Q factor (Q_{TLS}) at low power. In contrast, submersion in HF significantly improves Q_{TLS}, doubling its value. In Fig. 4(c), we present the distribution of Q_{TLS} values before and after each treatment across four different resonators, substantiating a decrease in resonator losses upon HF immersion, due to a twofold decrease of peak B. Extending the HF immersion to 10 min does not result in a reduction in spin density or a significant improvement in Q_{TLS}. However, it is intriguing that the annealing-induced reduction of spins corresponding to the sharper peak A does not improve the Q factor.

IV. DISCUSSION

The microscopic nature of the radicals that contribute to $g = 2$ peaks remains uncertain, as it is a characteristic of multiple different spin systems with free-electron-like g factors. However, the surface treatments can provide insights about the nature of the two spin groups. Numerous plausible candidates could give rise to these spins—e.g., the (001) surface of silicon is known to harbor numerous paramagnetic defects with g factors close to 2 [32]. These could manifest as dangling bonds in the Si-SiO_2 interface (P_b centers) [33,34], oxide trapping centers [32], and defects in oxides of niobium [8,35], among other possibilities. Previous reports indicate that P_{b0} centers (i.e., dangling bonds with trivalent silicon) dominate the interface traps at the (100) Si-SiO_2 boundary [34,36]. Annealing the sample results in the migration and rearrangement of these defects and therefore leads to surface passivation, reducing the ESR signal. Such a reduction in amorphous silicon has been observed previously [36] and corroborates our results. While other sources of $g = 2$ spins are not ruled out our findings from surface treatments suggest that these dangling-bond defects are primarily accountable for the sharper peak A.

The existence of the wider peak B, which responds differently to surface treatments, is more intriguing. The reduction in type-B spins after annealing is modest but after HF immersion it is significant, which suggests that these spins are likely located within the oxide layer on silicon. Recent studies have revealed that niobium oxides are removed at a much slower pace (2.2 pm/s) than silicon oxides (1.8 nm/s) [35]. Since the type-B spins show only a minor or no reduction after 10 min in HF, they are unlikely to be found within the niobium oxides. Furthermore, the absence of a similar broad peak in the NbN-on-sapphire spectrum leads us to discount the possibility of spins located exclusively at the NbN-air interface.

We note another interesting observation regarding the background signal. While the $g = 2$ peak appears around 162 mT for the 4.47-GHz resonator, the pedestal peaks at precisely half the field, i.e., at 81 mT [Fig. 3(a)]. As shown in Appendix E (Fig. 8), at elevated microwave powers, once the background signal is effectively suppressed, one can resolve a Gaussian peak at around 80 mT. This observation suggests that the background signal partially originates from spins with $S = 1$. This may be attributed to spin-spin interactions and clustering of spins, resulting in the formation of spin-triplet centers. These

mechanisms are considered potential contributors to $1/f$ flux noise [37,38].

The impact of treatments on Q_{TLS} offers additional insights into the nature of spin ensembles. Within the framework of the GTM, coherent TLSs (cTLSs) that are resonant with the resonator engage in energy exchange and dissipation into the surrounding environment, leading to energy loss in resonators. On the other hand, the interaction of coherent TLSs with a bath of thermally activated TLFs leads to spectral drift of the resonant frequency, a key factor contributing to its temporal fluctuations [10,15].

The negligible reduction in loss ($1/Q_i$) observed upon annealing, coupled with a dramatic decrease in the density of the type-A spins suggests that, while these spins are removed, they do not affect the density of the cTLSs. Most of the commonly discussed spin radicals in literature, such as dangling bonds, adatoms, defects, and vacancies, are known to exhibit both spin and charge (or electric dipole) characteristics [32,36]. Previous findings in sapphire have confirmed that desorption of the spins does not result in a significant improvement of loss but leads to a tenfold reduction in noise, indicating that the spins on sapphire function as classical TLFs [10]. Our observations and similar findings in Ref. [10] suggest that dipoles associated with type-A spins function as classical TLFs, although resonator-noise measurements are required to verify this assertion. Immersion in HF, however, reduces the TLS losses by a factor of 2 and concurrently reduces the density of type-B spins by the same factor (Fig. 4). This implies that type-B spins are associated with coherent two-level systems and are of a distinct nature compared to the type-A spins. Hence, despite having similar g factors, the two spin species have different origins and different influences on decoherence.

We also highlight that type-B spins exhibit a significantly wider peak (smaller T_{2e}) compared to type-A spins. We speculate that this difference may be attributed to the fact that TLS-related dissipation comes from near-resonant charge fluctuations and under the ESR resonance condition, the spins of those TLSs also come into resonance with the microwave field. This concurrent near resonance of both the spins and associated charges of type-B radicals should coherently couple spins and charges through photons. This exotic interaction has not been explored in the existing literature, particularly in relation to decoherence mechanisms, and we hope that our findings will stimulate further work in this direction.

V. CONCLUSIONS

In conclusion, our study sheds light on the presence and impact of surface spins on silicon substrates in the context of superconducting quantum systems. Using an on-chip ESR technique, we have identified two distinct groups of spins, each demonstrating a unique response to power variations and surface treatments. We have reduced the density of paramagnetic spins by a factor of between 3 and 5, which we anticipate will significantly decrease both flux and charge noise levels. Our study categorizes "type-A" spins as plausible incoherent two-level fluctuators, known contributors to charge noise and to energy shifts in coherent TLSs. Conversely, "type-B" spins seem to be linked with coherent TLSs on the silicon surface, directly influencing resonator loss. Therefore, a combination of ESR spectroscopy with measurements of energy loss has been instrumental in distinguishing between coherent and incoherent fluctuators in silicon-based quantum circuits. By employing advanced spectroscopic techniques such as electron-nuclear double resonance (ENDOR) and electron-electron double resonance (ELDOR), one can acquire intricate details about the elemental and structural composition of TLS and/or TLF hosts (cf. Ref. [26]) thereby offering promising avenues for informed noise and decoherence mitigation in quantum systems.

ACKNOWLEDGMENTS

We are grateful for discussions with Anita Fadavi Roudsari, Amr Osman, and Janka Biznárová. This work was performed in part at Myfab Chalmers. We acknowledge support from the Knut and Alice Wallenberg Foundation via the Wallenberg Center for Quantum Technology (WACQT), the Horizon Europe EIC Pathfinder project 101115190 IQARO, and from the EU Flagship on Quantum Technology HORIZON-CL4-2022-QUANTUM-01-SGA project 101113946 OpeSuperQPlus100. S.K. and A.D. acknowledge the support from the Swedish Research Council (VR) (Grant Agreements No. 2019-05480 and No. 2020-04393).

APPENDIX A: METHODS

The resonators have been fabricated on a high-resistivity ($\rho > 10$ kΩ cm) intrinsic silicon (100) substrate. The substrate has been dipped in 2% HF solution to remove native oxide and then subsequently rinsed with deionized water. The wafer has then immediately been loaded into a metal sputter chamber. Before the deposition of NbN, the samples have been annealed *in situ* at 600 °C for 20 min and a 2-nm seed layer has been deposited. After being cooled to room temperature, an additional 120 nm of NbN has been sputtered. The resonators have then been patterned using electron-beam lithography (UV60 resist: 33 $\mu C/cm^2$ dose, MF-CD-26 developer, rinse in deionized water) and have subsequently been etched in an Ar-Cl_2 plasma. The fabrication procedure is similar to that in Refs. [21,29].

All experiments have been conducted at a temperature of 300 mK using a ^{3}He single-shot refrigerator. After the initial measurements, the sample has been subjected to a series of surface treatments. First, it has been annealed in

a vacuum at 300 °C for 30 min and subsequently remeasured. Second, it has been immersed in a 5% HF solution for 60 s and then promptly reloaded into the cryostat within 45–60 min. This procedure has later been repeated but with the HF immersion time extended to 10 min.

APPENDIX B: LORENTZIAN FITS

In Fig. 5, we present the Lorentzian fits to the spectrum before and after surface treatments for two different resonators. To assess the accuracy of our fits, we have illustrated the residuals of the Lorentzian fits, which represent the discrepancies between the experimental and fitted data. We contrast the residuals obtained from a dual-Lorentzian fit (dark gray) with those from a single-Lorentzian fit (orange), demonstrating that fitting with two Lorentzians more precisely reflects the experimental data. These residuals are minimal (less than 5%) when compared to the experimental peak magnitude, affirming the accuracy of Lorentzian fits for both spin groups. The fidelity of dual-Lorentzian fitting suggests that homogeneous broadening mechanisms predominate for both spin species.

It is also evident from the figure that surface treatments result in a noticeable decrease in the amplitude of the peaks. However, the treatments cause little to no effect on the peak widths, suggesting that the T_2 relaxation time remains largely unchanged. Instead, this observation points to a reduction in the density of spins as the primary effect of the treatments.

APPENDIX C: POWER DEPENDENCE OF ESR PEAKS

The ESR spectra have been measured as a function of the microwave power, as shown in Fig. 6. With increasing power, a larger number of spins are driven out of equilibrium, which leads to diminished spin-induced dissipation [see Fig. 6(a)].

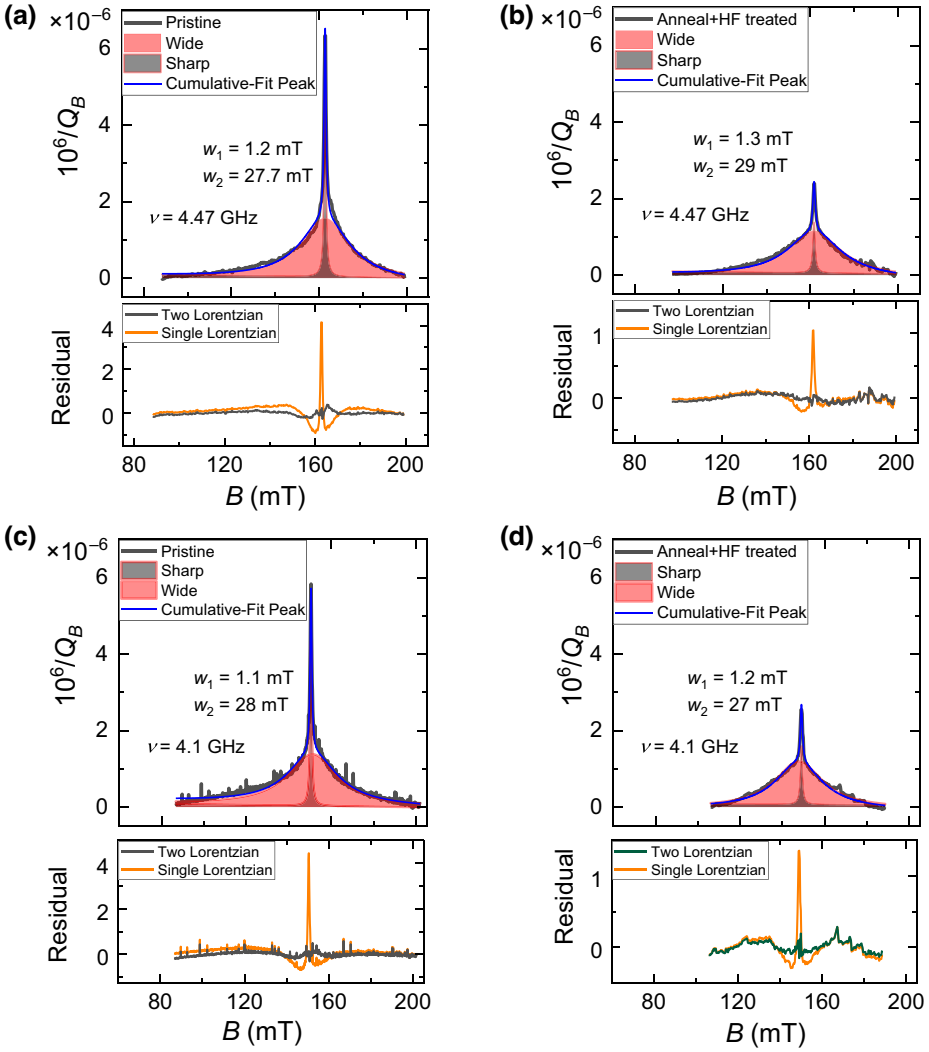

FIG. 5. The Lorentzian fitting of the central $g = 2$ peaks for (a),(b) a 4.47-GHz resonator and (c),(d) the 4.1-GHz resonator before and after surface treatments. All the fits are accompanied by their residuals (dark gray) and also compared with residuals of a single Lorentzian fit (orange).

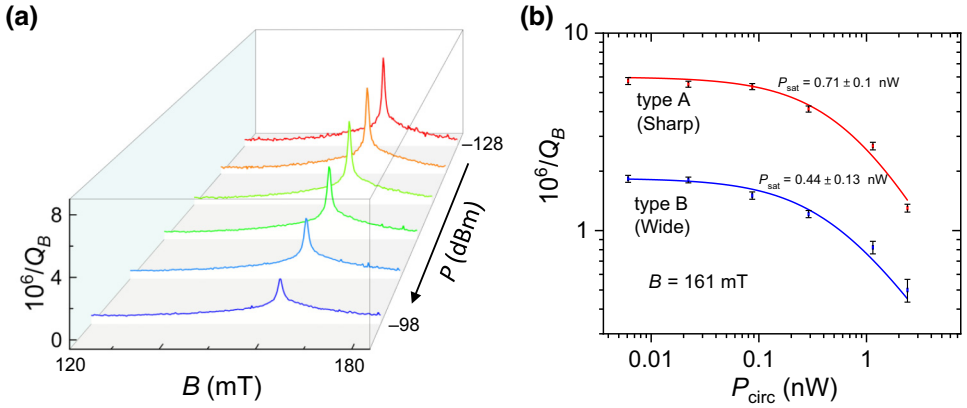

FIG. 6. (a) The ESR spectrum for various microwave drive powers at 300 mK. (b) The inverse of the quality factor associated with energy dissipation into each individual spin system as a function of the circulating power ($P_{\mathrm{circ}} = 2Q^2P_{\mathrm{drive}}/Q_c$), with fits to Eq. (C1).

By fitting two Lorentzian curves and decomposing the peak, we can extract the power dependence of spin-induced dissipation from individual species,

$$\frac{1}{Q_B(P)} = \frac{1}{Q_{B0}}\left(\frac{1}{1+P/P_{\mathrm{sat}}}\right)^{\epsilon}, \tag{C1}$$

where the saturation power is $P_{\mathrm{sat}} = 1/T_{1e}T_2\gamma_e^2\alpha^2$, $\epsilon \sim 1$ is the inhomogeneity parameter describing how quickly spins saturate to increasing power [39], γ_e is the gyromagnetic ratio, and $\alpha = H/\sqrt{P_0}$ is the microwave power to microwave magnetic field conversion coefficient. An approximate value for our resonator, considering two parallel superconducting strips, is $\alpha = 0.21\ \mathrm{T}/\sqrt{\mathrm{W}}$ [21].

The saturation power for type-A spins is 0.71 ± 0.1 nW and for type-B spins it is 0.44 ± 0.13 nW. Given that peak B has a shorter relaxation time scale (T_2), it is anticipated to relax at a higher power in comparison to the sharp peak. However, in our observations, both type-A and type-B spins saturate at approximately the same power, within the margins of error.

In our work, all ESR spectra have been obtained at power levels below the saturation threshold ($P < P_{\mathrm{sat}}$), ensuring nonsaturating conditions throughout the measurements.

APPENDIX D: EFFECT OF HF TREATMENT WITHOUT ANNEALING PROCEDURE

In the majority of samples, HF treatment has been carried out after the annealing procedure. This has resulted in enhancements in the Q factor and a decrease in the amplitude of the wide peak. To decouple the effects of annealing and HF treatment, we have measured the ESR spectrum of a sample treated with HF for 60 s without preceding annealing (Fig. 7). The results are consistent with our previous samples treated with HF after annealing: there is a minor reduction in the area of the sharp peak, a twofold

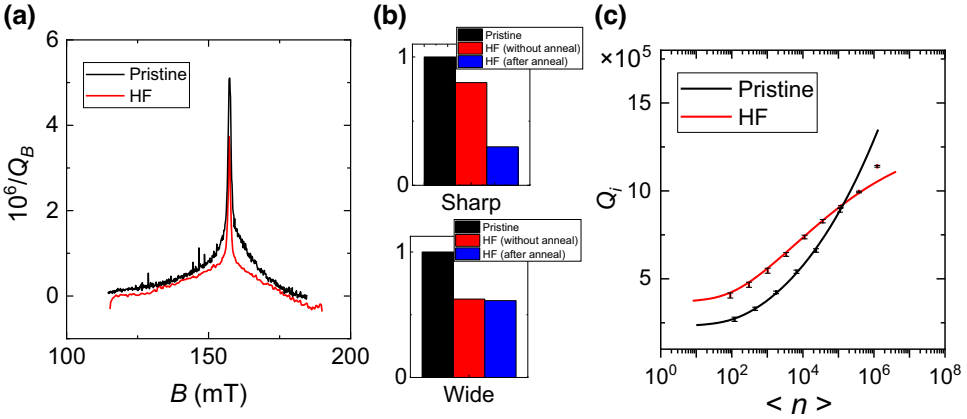

FIG. 7. (a) The ESR spectra of the 4.47-GHz resonator before and after HF treatment for 60 s. This sample has not been subjected to annealing. (b) Minor reduction in the normalized area of peak A and twofold reduction of peak B after HF treatment. The area is compared to the HF-treated sample after annealing. (c) Q_i versus $\langle n \rangle$, showing a corresponding twofold improvement in Q_{TLS}.

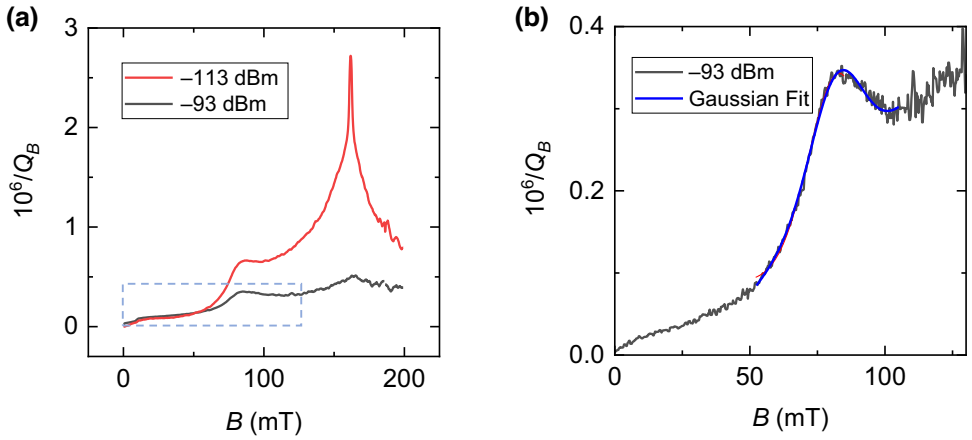

FIG. 8. (a) The ESR spectrum of the sample following surface treatments, at both lower and higher microwave power levels. (b) An enlarged view of the high-power spectrum, revealing the peak at half the field value of the $g = 2$ peak (approximately 80 mT), which has been distinctly resolved and fitted with a Gaussian function.

reduction in the area of the broad peak, and a corresponding twofold improvement in Q_{TLS}. These findings suggest that the impacts of HF treatment are independent of those stemming from annealing.

The high power (radiation-limited) loss in our resonator (δ_0), however, does not show a consistent improvement with surface treatment. This can be attributed to different configurations of the wire bonds to the ground plane while rebonding after treatment. It is known that such configurations can inadvertently change the electromagnetic environment and introduce parasitic modes within the ground plane, resulting in additional loss channels that adversely impact the overall performance of the resonator at higher circulating powers.

APPENDIX E: ESR BACKGROUND SPECTRUM AND $S = 1$ PEAK

In Fig. 8(a), we show the ESR spectrum of the 4.47-GHz resonator after surface treatments at two different driving microwave powers. At higher power, both peaks corresponding to $g = 2$ spins are effectively suppressed, along with a significant reduction in the background signal, as a result of spin saturation. Once the background noise is substantially reduced, a distinct peak becomes observable at approximately 80 mT, which is half the field strength typically associated with $g = 2$ spins ($S = 1/2$). This peak is indicative of the double quantum magnetic transition, which is typically forbidden in a noninteracting spin system but becomes permissible with a finite probability in the presence of dipolar interactions [40]. It is therefore a hallmark of triplet-state systems with $S = 1$ and is believed to emerge from the interactions among electron spins and spin clustering [37,40]. The resolved peak can be reliably fitted with a Gaussian function with a line width of 20 mT. This suggests that the peak is inhomogeneously broadened, as illustrated in Fig. 8(b).

[1] E. Paladino, Y. M. Galperin, G. Falci, and B. L. Altshuler, $1/f$ noise: Implications for solid-state quantum information, Rev. Mod. Phys. **86**, 361 (2014).
[2] J. Burnett, L. Faoro, I. Wisby, V. L. Gurtovoi, A. V. Chernykh, G. M. Mikhailov, V. A. Tulin, R. Shaikhaidarov, V. Antonov, P. J. Meeson, A. Y. Tzalenchuk, and T. Lindström, Evidence for interacting two-level systems from the $1/f$ noise of a superconducting resonator, Nat. Commun. **5**, 4119 (2014).
[3] C. Müller, J. H. Cole, and J. Lisenfeld, Towards understanding two-level-systems in amorphous solids: Insights from quantum circuits, Rep. Prog. Phys. **82**, 124501 (2019).
[4] C. Wang, C. Axline, Y. Y. Gao, T. Brecht, Y. Chu, L. Frunzio, M. H. Devoret, and R. J. Schoelkopf, Surface participation and dielectric loss in superconducting qubits, Appl. Phys. Lett. **107**, 162601 (2015).
[5] P. Macha, S. H. W. van der Ploeg, G. Oelsner, E. Il'ichev, H.-G. Meyer, S. Wünsch, and M. Siegel, Losses in coplanar waveguide resonators at millikelvin temperatures, Appl. Phys. Lett. **96**, 062503 (2010).
[6] J. M. Gambetta, C. E. Murray, Y.-K.-K. Fung, D. T. McClure, O. Dial, W. Shanks, J. W. Sleight, and M. Steffen, Investigating surface loss effects in superconducting transmon qubits, IEEE Trans. Appl. Supercond. **27**, 1 (2017).
[7] A. Osman, J. Fernández-Pendás, C. Warren, S. Kosen, M. Scigliuzzo, A. Frisk Kockum, G. Tancredi, A. Fadavi Roudsari, and J. Bylander, Mitigation of frequency collisions in superconducting quantum processors, Phys. Rev. Res. **5**, 043001 (2023).
[8] J. Verjauw, A. Potočnik, M. Mongillo, R. Acharya, F. Mohiyaddin, G. Simion, A. Pacco, T. Ivanov, D. Wan, A. Vanleenhove, L. Souriau, J. Jussot, A. Thiam, J. Swerts, X. Piao, S. Couet, M. Heyns, B. Govoreanu, and I. Radu,

Investigation of microwave loss induced by oxide regrowth in high-Q niobium resonators, Phys. Rev. Appl. **16**, 014018 (2021).

[9] J. Lisenfeld, A. Bilmes, A. Megrant, R. Barends, J. Kelly, P. Klimov, G. Weiss, J. M. Martinis, and A. V. Ustinov, Electric field spectroscopy of material defects in transmon qubits, npj Quantum Inf. **5**, 1 (2019).

[10] S. E. de Graaf, L. Faoro, J. Burnett, A. A. Adamyan, A. Y. Tzalenchuk, S. E. Kubatkin, T. Lindström, and A. V. Danilov, Suppression of low-frequency charge noise in superconducting resonators by surface spin desorption, Nat. Commun. **9**, 1143 (2018).

[11] L. Faoro and L. B. Ioffe, Internal loss of superconducting resonators induced by interacting two-level systems, Phys. Rev. Lett. **109**, 157005 (2012).

[12] J. J. Burnett, A. Bengtsson, M. Scigliuzzo, D. Niepce, M. Kudra, P. Delsing, and J. Bylander, Decoherence benchmarking of superconducting qubits, npj Quantum Inf. **5**, 1 (2019).

[13] J. M. Martinis, K. B. Cooper, R. McDermott, M. Steffen, M. Ansmann, K. D. Osborn, K. Cicak, S. Oh, D. P. Pappas, R. W. Simmonds, and C. C. Yu, Decoherence in Josephson qubits from dielectric loss, Phys. Rev. Lett. **95**, 210503 (2005).

[14] M. Lucas, A. V. Danilov, L. V. Levitin, A. Jayaraman, A. J. Casey, L. Faoro, A. Y. Tzalenchuk, S. E. Kubatkin, J. Saunders, and S. E. de Graaf, Quantum bath suppression in a superconducting circuit by immersion cooling, Nat. Commun. **14**, 3522 (2023).

[15] L. Faoro and L. B. Ioffe, Interacting tunneling model for two-level systems in amorphous materials and its predictions for their dephasing and noise in superconducting microresonators, Phys. Rev. B **91**, 014201 (2015).

[16] P. Kumar, S. Sendelbach, M. A. Beck, J. W. Freeland, Z. Wang, H. Wang, C. C. Yu, R. Q. Wu, D. P. Pappas, and R. McDermott, Origin and reduction of $1/f$ magnetic flux noise in superconducting devices, Phys. Rev. Appl. **6**, 041001(R) (2016).

[17] S. M. Anton, J. S. Birenbaum, S. R. O'Kelley, V. Bolkhovsky, D. A. Braje, G. Fitch, M. Neeley, G. C. Hilton, H.-M. Cho, K. D. Irwin, F. C. Wellstood, W. D. Oliver, A. Shnirman, and J. Clarke, Magnetic flux noise in dc squids: Temperature and geometry dependence, Phys. Rev. Lett. **110**, 147002 (2013).

[18] C. M. Quintana, *et al.*, Observation of classical-quantum crossover of $1/f$ flux noise and its paramagnetic temperature dependence, Phys. Rev. Lett. **118**, 057702 (2017).

[19] S. K. Choi, D. H. Lee, S. G. Louie, and J. Clarke, Localization of metal-induced gap states at the metal-insulator interface: Origin of flux noise in squids and superconducting qubits, Phys. Rev. Lett. **103**, 197001 (2009).

[20] R. de Sousa, Dangling-bond spin relaxation and magnetic $1/f$ noise from the amorphous-semiconductor/oxide interface: Theory, Phys. Rev. B **76**, 245306 (2007).

[21] S. E. de Graaf, A. A. Adamyan, T. Lindström, D. Erts, S. E. Kubatkin, A. Y. Tzalenchuk, and A. V. Danilov, Direct identification of dilute surface spins on Al_2O_3: Origin of flux noise in quantum circuits, Phys. Rev. Lett. **118**, 057703 (2017).

[22] H. Wang, C. Shi, J. Hu, S. Han, C. C. Yu, and R. Q. Wu, Candidate source of flux noise in squids: Adsorbed oxygen molecules, Phys. Rev. Lett. **115**, 077002 (2015).

[23] N. Adelstein, D. Lee, J. L. DuBois, K. G. Ray, J. B. Varley, and V. Lordi, Magnetic stability of oxygen defects on the SiO_2 surface, AIP Adv. **7**, 025110 (2017).

[24] S. LaForest and R. de Sousa, Flux-vector model of spin noise in superconducting circuits: Electron versus nuclear spins and role of phase transition, Phys. Rev. B **92**, 054502 (2015).

[25] S. E. de Graaf, L. Faoro, L. B. Ioffe, S. Mahashabde, J. J. Burnett, T. Lindström, S. E. Kubatkin, A. V. Danilov, and A. Y. Tzalenchuk, Two-level systems in superconducting quantum devices due to trapped quasiparticles, Sci. Adv. **6**, eabc5055 (2020).

[26] S. Un, S. de Graaf, P. Bertet, S. Kubatkin, and A. Danilov, On the nature of decoherence in quantum circuits: Revealing the structural motif of the surface radicals in α-Al_2O_3, Sci. Adv. **8**, eabm6169 (2022).

[27] S. E. de Graaf, D. Davidovikj, A. Adamyan, S. E. Kubatkin, and A. V. Danilov, Galvanically split superconducting microwave resonators for introducing internal voltage bias, Appl. Phys. Lett. **104**, 052601 (2014).

[28] S. E. de Graaf, A. V. Danilov, A. Adamyan, T. Bauch, and S. E. Kubatkin, Magnetic field resilient superconducting fractal resonators for coupling to free spins, J. Appl. Phys. **112**, 123905 (2012).

[29] S. Mahashabde, E. Otto, D. Montemurro, S. de Graaf, S. Kubatkin, and A. Danilov, Fast tunable high-Q-factor superconducting microwave resonators, Phys. Rev. Appl. **14**, 044040 (2020).

[30] A. K. V. Keyser, J. J. Burnett, S. E. Kubatkin, A. V. Danilov, M. Oxborrow, S. E. de Graaf, and T. Lindström, Pulsed electron spin resonance of an organic microcrystal by dispersive readout, J. Magn. Reson. **321**, 106853 (2020).

[31] K. L. Brower and S. M. Myers, Chemical kinetics of hydrogen and (111) Si-SiO_2 interface defects, Appl. Phys. Lett. **57**, 162 (1990).

[32] P. M. Lenahan and J. F. Conley, Jr.What can electron paramagnetic resonance tell us about the Si/SiO_2 system? J. Vac. Sci. Technol. B **16**, 2134 (1998).

[33] P. J. Caplan, E. H. Poindexter, B. E. Deal, and R. R. Razouk, ESR centers, interface states, and oxide fixed charge in thermally oxidized silicon wafers, J. Appl. Phys. **50**, 5847 (1979).

[34] E. H. Poindexter, G. J. Gerardi, M.-E. Rueckel, P. J. Caplan, N. M. Johnson, and D. K. Biegelsen, Electronic traps and Pb centers at the Si/SiO_2 interface: Band-gap energy distribution, J. Appl. Phys. **56**, 2844 (1984).

[35] M. V. P. Altoé, A. Banerjee, C. Berk, A. Hajr, A. Schwartzberg, C. Song, M. Alghadeer, S. Aloni, M. J. Elowson, J. M. Kreikebaum, E. K. Wong, S. M. Griffin, S. Rao, A. Weber-Bargioni, A. M. Minor, D. I. Santiago, S. Cabrini, I. Siddiqi, and D. F. Ogletree, Localization and mitigation of loss in niobium superconducting circuits, PRX Quantum **3**, 020312 (2022).

[36] I. Ohdomari, M. Kakumu, H. Sugahara, M. Hori, T. Saito, T. Yonehara, and Y. Hajimoto, Electron paramagnetic resonance study on the annealing behavior of vacuum deposited

amorphous silicon on crystalline silicon, J. Appl. Phys. **52**, 6617 (1981).

[37] R. C. Stevenson, Triplet state EPR spectra, J. Magn. Reson. (1969) **57**, 24 (1984).

[38] J. Atalaya, J. Clarke, G. Schön, and A. Shnirman, Flux $1/f^{\alpha}$ noise in two-dimensional heisenberg spin glasses: Effects of weak anisotropic interactions, Phys. Rev. B **90**, 014206 (2014).

[39] D. A. Haas, C. Mailer, and B. H. Robinson, Using nitroxide spin labels. How to obtain T_{1e} from continuous wave electron paramagnetic resonance spectra at all rotational rates, Biophys. J **64**, 594 (1993).

[40] P. Bertrand, *Electron Paramagnetic Resonance Spectroscopy: Fundamentals* (Springer Nature, Cham, Switzerland, 2020). The Zero-Field Splitting Term. EPR Spectrum for Paramagnetic Centres of Spin Greater than $1/2$.